Displacement field of a screw dislocation in a ⟨ 011 ⟩ Cu nanowire: An atomistic study

Marc Gailhanou, Jean-Marc Roussel

Displacement field of a screw dislocation in a ⟨011⟩ Cu nanowire: An atomistic study

Marc Gailhanou and Jean-Marc Roussel
IM2NP, UMR 7334 CNRS, Aix-Marseille Université, Faculté des Sciences et Techniques de Saint-Jérôme, Service 262, F-13397 Marseille Cedex 20, France
(Received 3 August 2013; published 10 December 2013)

By performing atomistic calculations with a tight-binding potential, we study the displacement field induced by a screw dislocation lying along a free ⟨011⟩ Cu cylindrical nanowire. For this anisotropic orientation that is often encountered experimentally, we show that the displacement field u_z along the nanowire can be seen as the superposition of three different fields: the screw dislocation field in an infinite medium, the warping displacement field caused by the so-called Eshelby twist, and an additional image field induced by the free surfaces. A Fourier series analysis of this latter image displacement and stress fields is given. For a circular cross section of the wire, this image field corresponds mainly to an additional warping displacement $u_z \propto xy$. The dissociation mechanism of the dislocation into partials and the surface stress effects being also captured in our simulations, the present study enables one to quantify the various contributions to the formation of the x-ray diffractograms.

DOI: 10.1103/PhysRevB.88.224101 PACS number(s): 61.72.Bb, 81.07.Gf, 61.72.Dd

I. INTRODUCTION

The pioneering study of Eshelby[1–3] on the stability of a screw dislocation in a thin rod is an outstanding example[4] of a single line defect leading to a macroscopic torsion of the sample. This so-called Eshleby twist takes place to cancel the torque due to the screw dislocation and thus stabilizes the defect at the center of the twisted rod. The angle of twist per unit length of the bar depends on the intensity of the Burgers vector and the surface of the cross section of the cylindrical wire.

Recent experimental works have revealed spectacular superstructures directly related to the Eshelby twist.[5] Other studies based on sophisticated x-ray diffraction techniques are currently carried out to resolve the displacement field in these nanosystems.[6–8] One significant advance would be, for instance, to identify a single screw dislocation in a single nanowire in order to correlate the influence of this defect to the mechanical properties of the nanowire.

From a theoretical viewpoint, the full calculation of the displacement field in a nanowire containing a dislocation is also nontrivial since the question of the image displacement fields induced by the free surfaces has to be resolved. The metallic fcc nanowires are in general oriented along a ⟨011⟩ direction with an equilibrium shape made of {100} and {111} facets.[9] By twisting the wire[10] or during its growth, screw dislocation might nucleate along the nanowire. Various ingredients are to be accounted in this problem. First in metal, the perfect [011] screw dislocation dissociates into two partials separated by a distance that can be significant in comparison to the radius of the nanowire. This requires a description at the atomistic scale to capture the displacement field in this extended core.[11] Secondly, two types of anisotropic effects should be considered here, the anisotropy of the elastic constants leading to an angular dependence of the shear modulus in the cross-section plane and the anisotropy due to the shape of the wire. Finally, the influence of the surface stress on the boundary conditions should be also quantified in such a study where the nanowires have radii in the 10-nm range. As a result of these properties, the free surfaces induce an image displacement field that will be superposed to the dislocation and the torsion fields. In this work based on atomistic calculations we examine in detail the role of each of these components on the formation of the displacement field. More precisely, by solving the realistic case of an anisotropic Cu nanowire, three correlated questions are addressed: (i) Are the boundary conditions modified by the surface stress? (ii) Can we rationalize the atomic displacement field using elasticity theory? (iii) Can we expect a clear signature of the image field from an x-ray diffraction experiment?

The paper is organized as follows. First in Sec. II, we briefly introduce the modeling techniques employed and some important characteristics of the atomistic potential for the present study. Then using anisotropic elasticity, we recall the main theoretical arguments that explain how a screw dislocation can be stabilized along a ⟨011⟩ nanowire by the Eshelby twist. The problem of the boundary conditions is formulated by taking into account the presence of surface stress. In Sec. III, we show the results of our atomistic simulations on the displacement field that minimizes the elastic energy of a circular cylindrical nanowire containing an axial screw dislocation. In Sec. III A, we first study the influence of the surface stress on the boundary conditions on the lateral surfaces. Then in Sec. III B the image displacement field induced by the free lateral surface is analyzed in details using a Fourier series analysis. An analytical expression of the stress field for a circular nanowire is also proposed, in good agreement with the atomistic calculations. In Appendix B, we demonstrate the gain in energy of the image field from the first-order expansion term. The Fourier series method is extended to the case of a nanowire having the equilibrium hexagonal cross section. This more realistic case is successfully treated separately in Appendix A of this paper. Finally in Sec. III C, we analyze whether a coherent x-ray diffraction experiment made on one single nanowire would be sensitive to the image fields evidenced in this work.

II. MODEL

A. The SMA potential

The atomic interactions in Cu nanowire are described within the SMA potential derived from the second-moment

approximation of the density of states (DOS) in the tight-binding formalism.[12,13] This analytical potential was quite successful in predicting structural properties in pure fcc metals. The N-body character of the SMA potential gives, for instance, realistic vacancy formation energies, proper surface relaxations, and good elastic anisotropy when interactions are extended up to the second-neighbor atom distances. It is also well known that the second-moment approximation cannot reproduce the small value of the stacking fault energy that plays a crucial role on the dissociation distance of a screw dislocation. To capture this important quantity, higher-order moments of the DOS in the tight-binding model should be used. However, in the present study, to keep the analytical form of the SMA potential and to perform large-scale simulations, it was possible to bypass this limitation of the SMA potential by adjusting the cutoff interaction distance to get a realistic stacking fault energy. Details of this small modification are given below and consequences on the calculated bulk and surface properties are summarized here.

According to the SMA potential, the energy E_n of an atom on the site n having neighbor atoms on the sites m at distances r_{nm}, writes

$$E_n = -\beta\sqrt{\sum_m \exp\left[-2q\left(\frac{r_{nm}}{r_0}-1\right)\right]} + A\sum_m \exp\left[-p\left(\frac{r_{nm}}{r_0}-1\right)\right], \quad (1)$$

where A, β, p, q are the four parameters to be adjusted. r_0 is the first neighbor distance in the fcc metal structure. To perform molecular statics simulations within this type of semiempirical potentials, cutoff functions in Eq. (1) are generally introduced to avoid any discontinuities in energies and forces. The cutoff function consists of replacing the exponential terms in Eq. (1) by fifth-order polynomial forms for interaction distances r_{nm} greater than a threshold distance r_c to be chosen. In the present study, while keeping the values of the A, β, p, q, and r_0 parameters unchanged from previous studies on copper,[14,15] we increase r_c up to the third-nearest-neighbor distance. This enables one to get a positive stacking fault energy that is essential for the present study. Note for completeness that the interactions still vanish at the fourth-nearest-neighbor distance as in the previous parametrization.

B. Bulk and surface properties

The intrinsic stacking fault energy γ^{SF} plays an important role in the core dissociation of a screw dislocation into Shockley partials.[4,16] It contributes to maintain the two partials separated at a nanometer distance in copper. The modification made on r_c (i.e., $r_c = \sqrt{3}r_0$) in the present SMA potential leads to $\gamma^{\mathrm{SF}} \approx 55$ mJ m^{-2} (while 45 mJ m^{-2} is found experimentally[4] and the value of 44.4 mJ m^{-2} is obtained by Mishin *et al.*[17]). Classically,[4,16] the other physical constants that control the bulk dissociation length d_0 between the two partials are the norm of the Burgers vector $b = 2.5642$ Å and the $(\bar{1}1\bar{1})$ shear modulus $\mu_{(\bar{1}1\bar{1})}$. Within our slightly modified SMA potential, we get $\mu_{(\bar{1}1\bar{1})} = 46$ GPa for copper. This elastic coefficient should be compared to the usual 42 GPa given by other atomic potentials.[18] In the case of a free cylindrical nanowire having a radius of 300 Å, the dissociation distance obtained in our simulation is only a few tenths of Angströms greater than d_0 whose asymptotic value can be deduced from the dissociation distances $d(R)$ obtained for different radii R. Indeed, we find that $d(R) - d_0 \propto 1/R$ with a bulk d_0 value close to 14 Å.

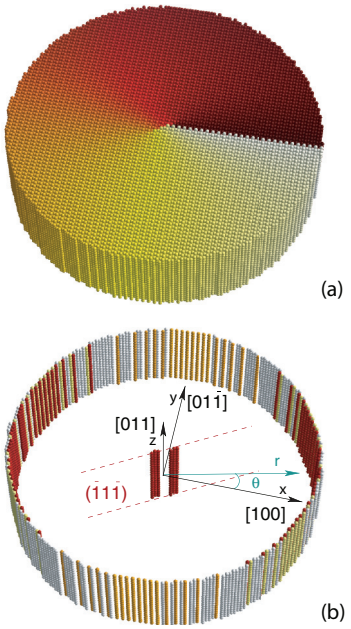

FIG. 1. (Color online) (a) Total displacement field u_z observed from our simulations (see text) for a circular [011] nanowire of radius 10 nm containing a screw dislocation. The color scale represents the u_z intensity ranging from 0 to b. (b) The two Schockley partials dissociated in the $(\bar{1}1\bar{1})$ plane and the twofold symmetry of the [011] orientation of the fcc nanowire are revealed by using an arbitrary color scale that draws atoms having high energy.

The typical simulation conditions considered in this work are the following and are illustrated in Fig. 1. We first build a perfect cylindrical fcc nanowire along a [011] direction with the desired cross-section shape. Then, a perfect screw dislocation, with Burgers vector $\boldsymbol{b} = 1/2\ a[011]$ is formed with the associated displacement field in an infinite isotropic medium (i.e., $u_z = u_z^{\infty,i} = b\theta/2\pi$). This simple initial configuration is then relaxed by performing quenched molecular dynamics simulations [also called molecular static (MS) calculations] to get the fully relaxed positions of the atoms in the structure and the corresponding energy at $T = 0$ K. To mimic an infinite free nanowire, torsion periodic boundary conditions are used in our simulations.[19] Since it is the torsion that stabilizes the screw dislocation into the wire, it is necessary for a given nanowire to perform a series of simulations with different torsions to determine the twist that minimizes the total energy of the system and defines the so-called Eshelby twist α_E (see Fig. 2). An other free variable to be examined is the contraction of the wire along its main z axis. Indeed, the undercoordinated surface atoms are in tension and they tend both to relax inward and to reduce the whole length of the nanowire. It results that bulk atoms are more and more in compression when the radius of nanowires decreases. In practice, we have parallelized our simulation code to run efficiently on graphics processing units

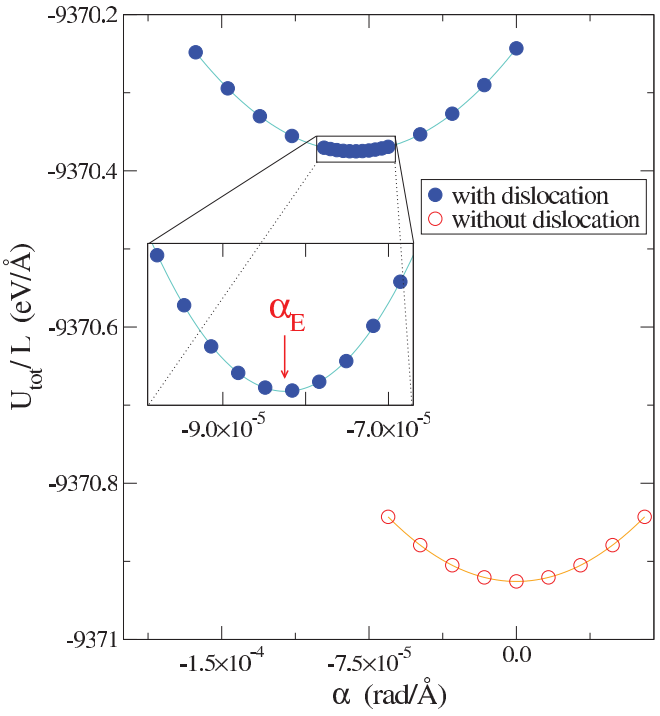

FIG. 2. (Color online) Atomistic calculations of the nanowire energy per unit length as a function of the applied torsion α in the two cases of a 10-nm radius nanowire containing a screw dislocation (solid circle) or not (open circle). With the dislocation, the minimum is shifted to a torsion value α_E that is called the Eshelby twist.

(GPU) and in order to consider simulation boxes containing up to one million atoms.

Figure 1 shows the metastable state reached after relaxation in our MS calculation at the Eshelby twist and the geometry of the system studied in this work. One of the two equivalent {111} planes is chosen [here $(\bar{1}1\bar{1})$] by the initial perfect screw dislocation to dissociate into two Schockley partials and thus to lower the energy. The Cartesian x, y, and z axes correspond, respectively, to the [100], [01$\bar{1}$], and [011] directions while in the cylindrical r,θ,z coordinates, θ is chosen to vanish along [100]. Figure 1 also shows a first representation of the total displacement field u_z observed from our simulations. At first glance, this latter seems to increase smoothly with θ. We will show in this work that in addition to this dominant isotropic tendency there are other important anisotropic contributions that will modify the x-ray diffraction, for instance. The anisotropy comes from the twofold symmetry of the [011] orientation of the fcc nanowire leading to inequivalent in-plane directions as it can be seen in Fig. 1 from the energies of the surface atoms.

It is worth noting that before reaching the metastable state made of the two parallel partials, we observe the formation and the annihilation of constrictions that are very similar to the ones discussed first by Rasmussen *et al.* (Ref. 11). Depending on the length of the nanowire and for the periodic conditions considered in this work, an even number of constrictions nucleates and leads to the splittings of the perfect screw dislocation into Shockley partials in the two different {111} glide planes. Then during the quenched molecular dynamics, constrictions are annihilated two by two. For an untwisted nanowire of radius 6 nm, the energies of the constrictions are very close to the ones obtained by Rasmussen *et al.* (i.e., in the present work: 3.35 eV for the edgelike and −1.10 eV for the screwlike). However, we also find in our simulations that the recombination energy decreases markedly with the torsion and increases for smaller radius of the nanowire.

To interpret the u_z displacement fields observed in this work, some specific surface and bulk elastic properties should be calculated within the SMA potential. First, since the nanowire axis coincides with the [011] twofold symmetry direction of the crystal and considering the x and y axis defined in Fig. 1 (belonging to the symmetry planes), the elastic constants C_{44}, C_{45}, and C_{55} are key terms to quantify the elastic energy in the twisted wire containing a screw dislocation. They can be obtained from the usual transformation rules by considering the elastic constants C^0_{11}, C^0_{12}, and C^0_{44} defined in the crystal axis coordinate system.[20] For the chosen {[100],[01$\bar{1}$],[011]} coordinate system, C_{45} vanishes and we find $C_{44} = (C^0_{11} - C^0_{12})/2 = 28$ GPa and $C_{55} = C^0_{44} = 82$ GPa in good agreement with the respective 26 GPa and 82 GPa experimental values.[21] In cylindrical coordinates, these elastic moduli can be written as

$$\begin{aligned} c_{44}(\theta) &= C_{\oplus} + C_{\ominus}\cos 2\theta, \\ c_{55}(\theta) &= C_{\oplus} - C_{\ominus}\cos 2\theta, \\ c_{45}(\theta) &= C_{\ominus}\sin 2\theta, \end{aligned} \tag{2}$$

with $C_{\oplus} = (C_{44} + C_{55})/2$ and $C_{\ominus} = (C_{44} - C_{55})/2$. The dependency with θ of Eq. (2) is plotted in Fig. 3(a) to underline the strong bulk anisotropy expected in ⟨011⟩ nanowires. This convenient representation is also used below to determine the components of the stress tensor.

A second source of anisotropy comes from the surface properties of the wire, namely the shape of the cross section and the variation of the surface stress along its contour. The shape of the cross section plays a key role in the elasticity boundary-value problem that is often nonintuitive but well documented. For instance, it is well known that the torsion of an anisotropic [011] bar with a circular section is analogous to the torsion of an isotropic [100] bar with an elliptical section and leads to the same warping displacement u_z.[2] In both situations, u_z is described by the same type of governing equation. More generally in the case of the circular anisotropic problem and for the out-of-plane displacements considered in this work,[22] the equilibrium equations reduce to the following expression:

$$C_{55}\frac{\partial^2 u_z}{\partial x^2} + C_{44}\frac{\partial^2 u_z}{\partial y^2} = 0. \tag{3}$$

For wires having a radius of nanosize, the effects of elastic surface properties (e.g., surface moduli and surface stress) should be examined in details to quantify the total strain energy. These questions have received lots of attention during these last decades since the pioneering mathematical works of Gurtin and Murdoch.[23–25] Using, for instance, the Chen *et al.*[26] approach, the surface stress is described as symmetric 2×2 tensor σ^S in the tangent plane of the curved surface. This latter is seen as a vanishingly thin membrane which can sustain in-plane stresses but offers no resistance for bending. Using force balance considerations, the derivation of the surface

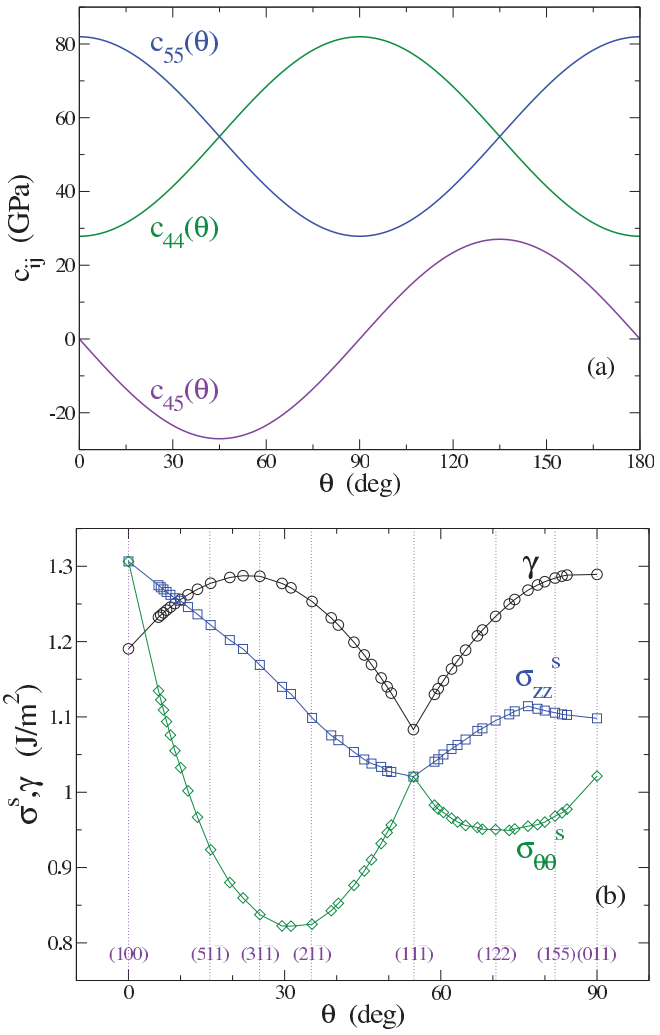

FIG. 3. (Color online) Bulk and surface anisotropy encountered in this work for a [011] copper nanowire described within the SMA potential: (a) θ dependence of the shear elastic moduli $c_{44}(\theta)$, $c_{55}(\theta)$, and $c_{45}(\theta)$ according to Eq. (2) and (b) surface energy γ and surface stress components $\sigma^S_{\theta\theta}$ and σ^S_{zz} calculated from perfect slabs having various θ orientations.

boundary conditions leads to generalized Young-Laplace equations where some components of the bulk stress tensor σ are now related to σ^S and the curvature of the surface.[26] In the present case of an infinite circular nanowire of radius R, the surface boundary conditions for the cylindrical coordinate system (r,θ,z) write

$$\begin{aligned}\sigma_{rr}|_{r=R} &= -\frac{\sigma^S_{\theta\theta}}{R},\\ \sigma_{r\theta}|_{r=R} &= \frac{1}{R}\frac{\partial\sigma^S_{\theta\theta}}{\partial\theta},\\ \sigma_{rz}|_{r=R} &= \frac{1}{R}\frac{\partial\sigma^S_{\theta z}}{\partial\theta},\end{aligned} \tag{4}$$

where $\sigma^S_{\theta\theta}$ and $\sigma^S_{\theta z}$ do not depend on z here. Note that the right terms in Eq. (4) vanish for large R and the classical boundary conditions on the lateral surfaces are then recovered. To study the influence of σ^S on the total u_z displacement field from our atomistic simulations, we need first to calculate the stress tensors on each atom. This is straightforward within the SMA potential that preserves an analytical form of each components σ_{ij}.[27] Since we have slightly modified the characteristic of the SMA potential (i.e., $r_c = \sqrt{3}r_0$), the last quantities of interest to be calculated in this section are the surface energies γ and the surface stresses σ^S_{ij} as a function of the surface orientation. These calculations are performed from various slabs presenting unreconstructed (1×1) surfaces with different orientations. Moreover, in-plane boundary conditions are applied to fix the in-plane lattice parameter to the infinite crystal value. Thus, the slab mimics a semi-infinite crystal where the bulk stress is null. These calculations also account for the usual inward atomic relaxation occurring at the surface. In Fig. 3(b), we report γ and the two diagonal surface tensor components σ^S_{zz} and $\sigma^S_{\theta\theta}$. The z direction corresponds to the [011] zone axis of the slab, and θ gives the surface orientation with respect to [001]. The trends shown in Fig. 3(b) are very similar to the ones already published with this type of potential.[28] Furthermore, by increasing r_c from $\sqrt{2}r_0$ to $\sqrt{3}r_0$, we observe (not shown here) that σ^S_{zz} and $\sigma^S_{\theta\theta}$ exhibit values that are globally enhanced (roughly by a factor ranging from 1.05 to 1.1) except for $\theta = 0$ where no change is noticed. Concerning γ the influence of r_c is also not pronounced and similar anisotropy is found.

C. The Eshelby twist in an anisotropic nanowire

The interaction between the screw dislocation and the lateral surface of the nanowire leads to a classical boundary problem.[3] Considering large radii where surface stress effects are neglected, the total stress field σ^{tot}_{ij} of a dislocation within a nanowire can be treated as three superimposed stress fields: the infinite stress field σ^{∞}_{ij} induced by the screw dislocation in an infinite crystal, a stress field $\sigma^{\text{twist}}_{ij}$ produced by the twist of the nanowire to cancel the torque due to the dislocation, and, finally, the image stress field σ^{img}_{ij} required to obtain a vanishing traction on the lateral surface. The total stress field inside the free twisted nanowire then writes

$$\sigma^{\text{tot}}_{ij} = \sigma^{\infty}_{ij} + \sigma^{\text{twist}}_{ij} + \sigma^{\text{img}}_{ij}, \tag{5}$$

where σ^{tot}_{ij} obey to the equilibrium equation that in the absence of body forces, writes

$$\frac{\partial\sigma^{\text{tot}}_{rz}}{\partial r} + \frac{1}{r}\frac{\partial\sigma^{\text{tot}}_{\theta z}}{\partial\theta} + \frac{1}{r}\sigma^{\text{tot}}_{rz} = 0. \tag{6}$$

Let us first recall the simplest case of an isotropic cylinder containing a coaxial screw dislocation.[4] The displacement $u^{\infty,i}_z$ (where the superscript i is for isotropic) is generally chosen as a linear function of θ, with associated stresses $\sigma^{\infty,i}_{\theta z}$ that can be written:

$$u^{\infty,i}_z = \frac{b\theta}{2\pi} = \frac{b}{2\pi}\tan^{-1}\frac{y}{x} \quad \sigma^{\infty,i}_{\theta z} = \frac{\mu b}{2\pi r}. \tag{7}$$

The Eshelby twist that minimizes the elastic energy writes

$$\alpha_E = -\frac{b}{\pi R^2}. \tag{8}$$

It produces displacements and stresses given by

$$u^{\text{twist,i}}_{\theta} = \alpha_E r z \quad \sigma^{\text{twist,i}}_{\theta z} = \mu\alpha_E r. \tag{9}$$

For a circular cross section the boundary conditions on the lateral surface can be expressed as

$$\sigma_{rr}^{\text{tot}}\big|_{r=R} = \sigma_{r\theta}^{\text{tot}}\big|_{r=R} = \sigma_{rz}^{\text{tot}}\big|_{r=R} = 0, \tag{10}$$

and are satisfied without requiring any image stress ($\sigma_{ij}^{\text{img},i} = 0$). In the anisotropic case, however, this is no longer true. Additional image stresses are necessary to fulfill the condition of a vanishing traction at the surface as expressed in Eq. (10). Indeed for the same configuration of a coaxial screw dislocation with Burgers vector $\boldsymbol{b} = 1/2\ a[110]$, the displacement field becomes (with $C_{45} = 0$)

$$u_z^{\infty} = \frac{b}{2\pi}\tan^{-1}\sqrt{\frac{C_{55}}{C_{44}}}\frac{y}{x}, \tag{11}$$

leading to two nonzero $\sigma_{\theta z}^{\infty}$ and σ_{rz}^{∞} components that write

$$\begin{aligned}\sigma_{\theta z}^{\infty} &= \frac{b\sqrt{C_{44}C_{55}}}{2\pi r},\\ \sigma_{rz}^{\infty} &= \frac{b\sqrt{C_{44}C_{55}}}{4\pi r}\frac{(C_{44}-C_{55})\sin 2\theta}{C_{44}\cos^2\theta + C_{55}\sin^2\theta}.\end{aligned} \tag{12}$$

Concerning the torsion required to minimize the elastic energy, the same Eshelby twist [given by Eq. (8)] is necessary for the circular anisotropic case.[2] The anisotropic situation is, however, different since a warping displacement u_z^{twist} is now produced by the torsion. Indeed, for a circular cylinder and any torsion α, we have

$$u_\theta^{\text{twist}} = \alpha r z \quad u_z^{\text{twist}} = \frac{\alpha}{2}\frac{C_{55}-C_{44}}{C_{55}+C_{44}}r^2\sin 2\theta, \tag{13}$$

leading to a radial stress field with the sole component,

$$\sigma_{\theta z}^{\text{twist}} = \alpha\frac{2C_{44}C_{55}r}{C_{44}+C_{55}} \tag{14}$$

that fulfills the boundary conditions of Eq. (10).

Thus, in the presence of the stress fields σ_{ij}^{∞} and $\sigma_{ij}^{\text{twist}}$ given by Eqs. (12) and (14), the image stress field σ_{ij}^{img} to be resolved for a circular cross section should have the following properties. First, in order to satisfy the surface traction conditions of Eq. (10) where surface stress effect is neglected, the σ_{rz}^{img} component must take a value at $r = R$ that is opposite to the one of σ_{rz}^{∞} in Eq. (12):

$$\sigma_{rz}^{\text{img}}\big|_{r=R} + \sigma_{rz}^{\infty}\big|_{r=R} = 0. \tag{15}$$

Secondly, for any θ and r, a nonvanishing $\sigma_{\theta z}^{\text{img}}$ component appears from the equilibrium equation [Eq. (6)]. And finally, a second relation between σ_{rz}^{img} and $\sigma_{\theta z}^{\text{img}}$ is found to satisfy the compatibility that ensures that the displacement u_z^{img} is continuous and single valued. This latter can be obtained from the partial derivatives of u_z^{img} that can be written as a function of σ_{rz}^{img} and $\sigma_{\theta z}^{\text{img}}$ as follows:

$$\begin{aligned}\frac{\partial u_z^{\text{img}}}{\partial\theta} &= \frac{r}{C_{44}C_{55}}\left[\sigma_{\theta z}^{\text{img}}c_{55}(\theta) - \sigma_{rz}^{\text{img}}c_{45}(\theta)\right],\\ \frac{\partial u_z^{\text{img}}}{\partial r} &= \frac{1}{C_{44}C_{55}}\left[-\sigma_{\theta z}^{\text{img}}c_{45}(\theta) + \sigma_{rz}^{\text{img}}c_{44}(\theta)\right].\end{aligned} \tag{16}$$

Using Eq. (16), the equation of compatibility is simply established here by verifying that $\frac{\partial^2 u_z^{\text{img}}}{\partial\theta\partial r} = \frac{\partial^2 u_z^{\text{img}}}{\partial r\partial\theta}$. We have

$$\begin{aligned}&\sigma_{\theta z}^{\text{img}}c_{55}(\theta) - \sigma_{rz}^{\text{img}}c_{45}(\theta) + r\frac{\partial}{\partial r}\left[\sigma_{\theta z}^{\text{img}}c_{55}(\theta) - \sigma_{rz}^{\text{img}}c_{45}(\theta)\right]\\ &\quad = \frac{\partial}{\partial\theta}\left[-\sigma_{\theta z}^{\text{img}}c_{45}(\theta) + \sigma_{rz}^{\text{img}}c_{44}(\theta)\right].\end{aligned} \tag{17}$$

To summarize, we search the image displacement field u_z^{img} that gives the complete expression of the displacement u_z^{tot} along the nanowire axis resulting from the presence of the dislocation, the lateral surface, and the Eshelby twist. In terms of stress, this problem consists in solving the two relevant σ_{rz}^{img} and $\sigma_{\theta z}^{\text{img}}$ stress components that are solutions of both the equilibrium [Eq. (6)] and the compatibility [Eq. (17)] equations with an additional constrain on the value of σ_{rz}^{img} at the lateral free surface (at $r = R$). This latter surface traction condition takes different forms if one considers the surface stress effect [Eq. (4)] or not [Eq. (15)]. In the present work, the full solution u_z^{tot} of this problem is resolved by performing atomistic simulations. From a detailed analysis of these results, it will be possible to extract the unknown image field after having quantified the role of the surface stress in our simulations.

III. RESULTS

A. Surface stress effects

Classical elasticity does not treat intrinsic size dependence in the elastic solutions of defects in nanowire. To model possible size and surface stress effects, one has to account for the generalized Young-Laplace (GYL) relations expressed in Eq. (4) that modify the boundary conditions. The aim of this section is to both verify the GYL relations from our atomistic simulations and quantify the change induced by the surface stress on the two stress components (i.e., σ_{rz} and $\sigma_{\theta z}$) relevant in this work.

To enable the comparison with the continuous description and since the stress tensor per atom is directly known from the SMA potential, we adopt a coarse-grained method where each grain is formed by few atoms and presents an average stress. Grains have a typical size of 5 Å and are obtained by dividing the cylinder in concentric shells that are themselves divided in angular sectors.

Contrary to the perfect slabs in Fig. 3(b), the bulk stress is not null in the nanowire. This bulk contribution must be subtracted from the stress measured in a grain located at the surface in order to get the surface stress (that is defined as a surface excess quantity). In practice, for one column of grains along a radial direction (defined by θ), the desired stress difference is obtained from the two first adjacent grains near the surface. The area chosen to calculate σ_{zz}^{S}, $\sigma_{\theta\theta}^{S}$, and $\sigma_{\theta z}^{S}$ is the one occupied by the grain at the surface. Some moving average between neighbor grains are then performed.

To verify the validity of our method, we compare in Fig. 4(a) the diagonal components σ_{zz}^{S} and $\sigma_{\theta\theta}^{S}$ deduced from the slabs as in Sec. II B and the ones obtained from the lateral surface of the circular nanowire with radius $R = 30$ nm. Figure 4(a) indicates that the large size of the wire and its low bulk stress enable one to generate all the surface orientations with states

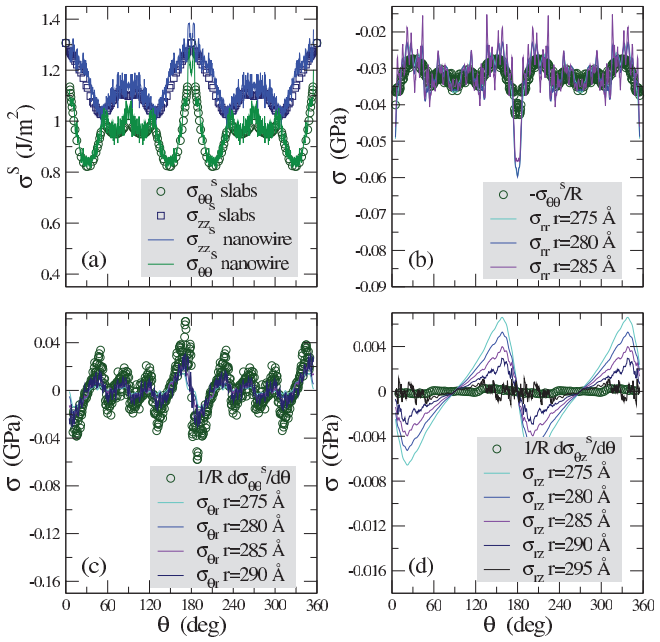

FIG. 4. (Color online) Test of the generalized Young-Laplace equations [Eq. (4)] at the lateral surface of a circular copper cylinder of radius $R = 30$ nm. (a) Comparison of the surface stress components σ^S_{zz} and $\sigma^S_{\theta\theta}$ calculated either from perfect slabs as in Fig. 3(b) or from a nanowire that is free of dislocation, then (b) the first, (c) the second, and (d) the third GYL equation are analyzed in the case of an untwisted nanowire containing the dislocation by comparing in Eq. (4) the θ dependence of the right surface terms to the respective left bulk terms calculated near the surface.

of stress that are close to the ones found from the slabs. The presence of steps on the nanowire surface and the choice of the grain size lead, however, to large fluctuations on the values of σ^S_{zz} and $\sigma^S_{\theta\theta}$.

In Figs. 4(b)–4(d), we wish to test the GYL equations in the case of the untwisted nanowire containing the screw dislocation. The first relation in Eq. (4) links $-\sigma^S_{\theta\theta}/R$ to $\sigma_{rr}|_{r=R}$ and simply means that a state of tension of the surface atoms leads to a radial compression of the bulk atoms that increases when R decreases. Along each column of grains defined by θ, we report in Fig. 4(b) how to vary σ_{rr} in grains close to the surface. Of course, the nonclassical GYL boundary conditions should be evidenced at the vicinity of the surface only. This is clearly the case in Fig. 4(b) where the variation of the $\sigma_{rr}|_{r\approx R}$ curve around -0.03 GPa is well reproduced by the $-\sigma^S_{\theta\theta}/R$ plot. One can recognize in particular on this figure the large $\sigma^S_{\theta\theta}$ value of the (100) surface (for $\theta = 0°$ and 180°) that induces a pronounced σ_{rr} near the surface. Similar conclusions are drawn for the two other GYL relations in Eq. (4) that are numerically demonstrated in Figs. 4(c) and 4(d) : near the surface for $r \approx R$, the bulk stress components $\sigma_{r\theta}|_{r\approx R}$ and $\sigma_{rz}|_{r\approx R}$ tend, respectively, to $\frac{1}{R}\frac{\partial\sigma^S_{\theta\theta}}{\partial\theta}$ and $\frac{1}{R}\frac{\partial\sigma^S_{\theta z}}{\partial\theta}$ where the θ derivatives of the surface σ^S components are performed from neighbor grains at the surface.

Only the third GYL equation [in Eq. (4)] involves σ_{rz} and therefore deserves a particular attention for the present work. Figure 4(d) shows that the variation of σ_{rz} (due to the dislocation as it will be shown in Sec. III B) is attenuated when r approaches R. According to the third GYL equation $\sigma_{rz}|_{r=R}$ should be equal to $\frac{1}{R}\frac{\partial\sigma^S_{\theta z}}{\partial\theta}$. The convergence of those two quantities can be seen on Fig. 4(d) when r tends to R. However, one can also observe that $\sigma_{rz}|_{r=R}$ is very small. Thus in the rest of this paper the boundary condition given by the third GYL equation will be considered as equivalent to the classical surface traction condition.

To summarize, we have shown from our atomistic calculations that the surface stress and the curvature of the lateral surface of the copper nanowire modify the classical boundary conditions as predicted by the GYL Eq. (4). These surface effects do not impact directly $\sigma_{\theta z}$ and our simulations show that they have a neglectable influence on σ_{rz} for the nanowires with large values of R such as the ones considered in this work ($6\text{ nm} < R < 30\text{ nm}$). Of course, we expect a more significant influence of the surface for thinner nanowires (for $R < 3$ nm) but at this scale the discretization effects, the high density of surface steps, and the dislocation core prevent the use of a continuous description of the stress in such small objects.

B. Image effects

To study the image field induced by the circular surface, we consider the case of a cylinder having a large radius of 30 nm as illustrated in Fig. 5. The color scale is the same for the four snapshots and represents the displacement field u_z along the [011] wire axis for different configurations. To compare the various fields, we first report in Fig. 5(a) the anisotropic solution [i.e., $u_z^\infty - u_z^{\infty,i}$ from Eqs. (7) and (11)] given for a screw dislocation in an infinite medium. Clearly from Fig. 5(a), but also from Fig. 6(a′) where values of $u_z^\infty - u_z^{\infty,i}$ are plotted as a function of θ, one can evaluate the importance of the anisotropy due to the high $C_{55} : C_{44}$ ratio in this system. The deviation from the isotropic field shown in Fig. 6(a′) can reach an amplitude of 0.1 Å and has no r dependence in this infinite crystal case.

The snapshot of Fig. 5(b) is obtained from our atomistic simulations in the case of an untwisted circular wire. The isotropic $u_z^{\infty,i}$ field is again subtracted to enable the comparison with Fig. 5(a). Figure 5(b) clearly reveals the importance of the image effects induced by the surface of the system. We observe that the image field tends to reinforce the anisotropy by a factor close to 2 at the vicinity of the surface where the u_z amplitude becomes maximum. To quantify this result, the corresponding u_z plot (denoted $u_z^\infty + u_z^{\text{img}} - u_z^{\infty,i}$) is shown in Fig. 6(b) while the image field u_z^{img} is extracted and reported in Fig. 6(b′). This latter graph confirms that near the surface u_z^{img} resembles to the displacement $u_z^\infty - u_z^{\infty,i}$. Figure 6(b′) also shows that the u_z^{img} amplitude decreases in the inner of the nanowire by following roughly a r^2 dependence.

In Figs. 5(c) and 6(c), we illustrate the case of a pure torsion of the nanowire without any dislocation. This atomistic MS simulation performed at the Eshelby twist of α_E [in Eq. (8)] gives rise to a warping displacement field (denoted u_z^{twist}) in very good agreement with the warping function u_z^{twist} expected from the elasticity theory and Eq. (13). This assertion will be demonstrated below in this section.

Finally in Figs. 5(d) and 6(d), we report the total displacement field u_z^{tot} due to both the presence of the screw dislocation

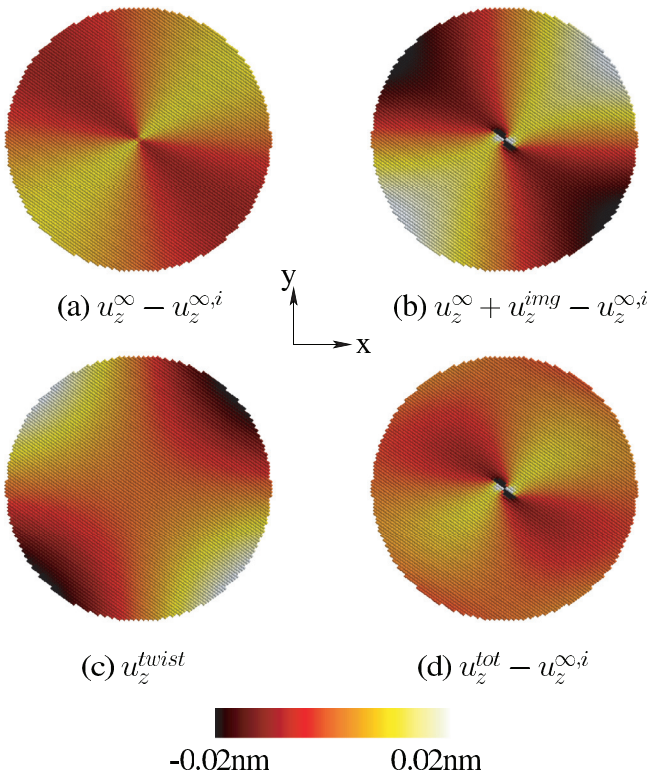

FIG. 5. (Color online) Color scale representation of the displacement field u_z in a [011] fcc circular nanowire of radius 30 nm: (a) Atoms are displaced according to the field difference $u_z^\infty - u_z^{\infty,i}$ between the anisotropic and the isotropic solutions of the screw ($b = 1/2\,a[110]$) dislocation in infinite fcc crystals; (b) displacement field (denoted $u_z^\infty + u_z^{\text{img}} - u_z^{\infty,i}$) obtained in our MS simulations from the fully relaxed positions of atoms in the case of an untwisted nanowire containing the screw dislocation. For comparison the solution $u_z^{\infty,i}$ is subtracted. (c) Atomistic MS simulation of the displacement field (denoted u_z^{twist}) resulting from the torsion at the Eshelby twist of the nanowire free of dislocation; (d) MS simulation of the atomic displacement ($u_z^{\text{tot}} - u_z^{\infty,i}$) in the case of the twisted nanowire containing the dislocation. This full solution corresponds well to the addition of (b) and (c).

and to the torsion of the nanowire that is necessary to cancel the torque induced by the defect. Interestingly, we find in our simulations that this latter angle of twist α agrees very well with the Eshelby's prediction α_E of Eq. (8) (we find $\alpha = -9.0968\ 10^{-6}$ rad/Å for $R = 30$ nm). The second important remark to be mentioned here concerns the superposition property of the displacement fields. Indeed, we verify that the displacement field obtained from the full simulation of a free circular nanowire containing a dislocation [in Fig. 5(d)] can be seen as the superposition of two separated contributions, i.e., the field resulting from the torsion of a perfect nanowire at the Eshelby twist [in Fig. 5(c)] and the field induced by the dislocation in an untwisted nanowire [in Fig. 5(b)]. In other words, we verify that $u_z^{\text{tot}} \approx u_z^\infty + u_z^{\text{img}} + u_z^{\text{twist}}$ meaning that (as expected from elasticity theory) to get u_z^{tot} one only needs to determine u_z^{img} in the untwisted case. This property comes from the circular cross section of the nanowire where the torsion field u_z^{twist} given by Eq. (13) already satisfies the lateral surface traction conditions of Eq. (10). Taking advantage of

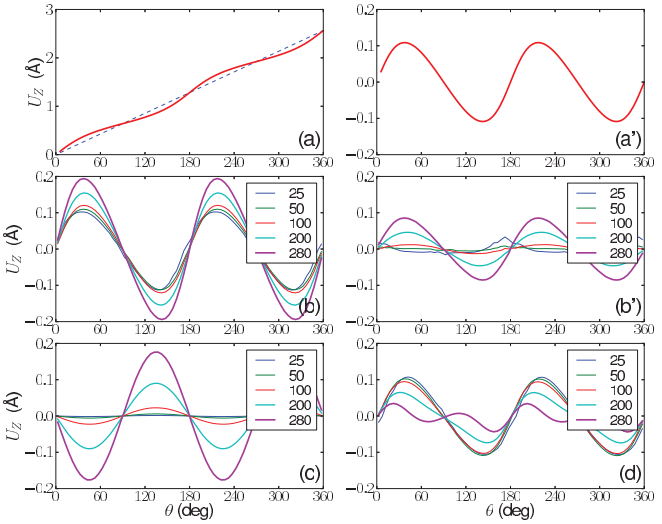

FIG. 6. (Color online) Angular dependence of the displacement field u_z calculated from the various configurations illustrated in Fig. 5. (a) First from the infinite crystal, the anisotropic and the isotropic solutions u_z^∞ and $u_z^{\infty,i}$ (dotted line) given by Eqs. (11) and (7) are plotted with in (a′) the difference $u_z^\infty - u_z^{\infty,i}$ corresponding to Fig. 5(a). Then, from our atomistic simulations in the [011] fcc circular nanowire of radius 30 nm, we report for different r values ranging from 25 to 280 Å. In (b) the displacement observed in Fig. 5(b) and denoted $u_z^\infty + u_z^{\text{img}} - u_z^{\infty,i}$, in (b′) the image field u_z^{img} extracted from (b) and (a′), in (c) the warping displacement u_z^{twist} due to the torsion as seen in Fig. 5(c), and finally in (d) the total displacement $u_z^{\text{tot}} - u_z^{\infty,i}$ found in the free nanowire Fig. 5(d).

this specificity of the circular cross section, we now focus on the modeling of $u_z^\infty + u_z^{\text{img}}$ found from the untwisted nanowire. $u_z^\infty + u_z^{\text{img}}$ is the solution of the equilibrium Eq. (3), that can take the following convenient expression in elliptic coordinates:

$$\frac{1}{r_e}\frac{\partial}{\partial r_e}\left(r_e \frac{\partial u_z}{\partial r_e}\right) + \frac{1}{r_e^2}\frac{\partial^2 u_z}{\partial \theta_e^2} = 0, \tag{18}$$

with $\theta_e = \arctan(C_\oslash^{1/2} y/x)$, $r_e^2 = r^2(C_\oslash^{-1/2}\cos^2\theta + C_\oslash^{1/2}\sin^2\theta)$, and $C_\oslash = C_{55}/C_{44}$. Considering the twofold symmetry, we seek a solution of Eq. (18) that writes

$$u_z^\infty + u_z^{\text{img}} = \frac{b}{2\pi}\theta_e + \sum_{n=1}^{N} A(n) r_e^{2n} \sin 2n\theta_e, \tag{19}$$

where values of the $A(n)$ Fourier coefficients are fixed by the surface traction condition.

Using $u_z^\infty + u_z^{\text{img}}$ in Eq. (19) we deduce the corresponding stress components $\sigma_{rz}^\infty + \sigma_{rz}^{\text{img}}$ and $\sigma_{\theta z}^\infty + \sigma_{\theta z}^{\text{img}}$ via the strain components that reduce here to $\epsilon_{\theta z} = \frac{1}{2r}\frac{\partial u_z}{\partial \theta}$ and $\epsilon_{rz} = \frac{1}{2}\frac{\partial u_z}{\partial r}$ with the relation, $\sigma_{\theta z} = 2c_{44}(\theta)\epsilon_{\theta z} + 2c_{45}(\theta)\epsilon_{rz}$ and $\sigma_{rz} = 2c_{55}(\theta)\epsilon_{rz} + 2c_{45}(\theta)\epsilon_{\theta z}$. Once the $A(n)$ dependence of $\sigma_{rz}^\infty + \sigma_{rz}^{\text{img}}$ is established from Eq. (19), it is straightforward to get numerically the $A(n)$ coefficients by applying the surface constrain $\sigma_{rz}^{\text{img}}|_{r=R} + \sigma_{rz}^\infty|_{r=R} = 0$ given in Eq. (15). From the determination of the $A(n)$, one obtains a full modeling of both the displacement and the stress fields, that can be directly compared to our atomistic simulations. This is illustrated in Fig. 7, where $\sigma_{rz}^\infty + \sigma_{rz}^{\text{img}}$ and $\sigma_{\theta z}^\infty + \sigma_{\theta z}^{\text{img}}$ fields are plotted for

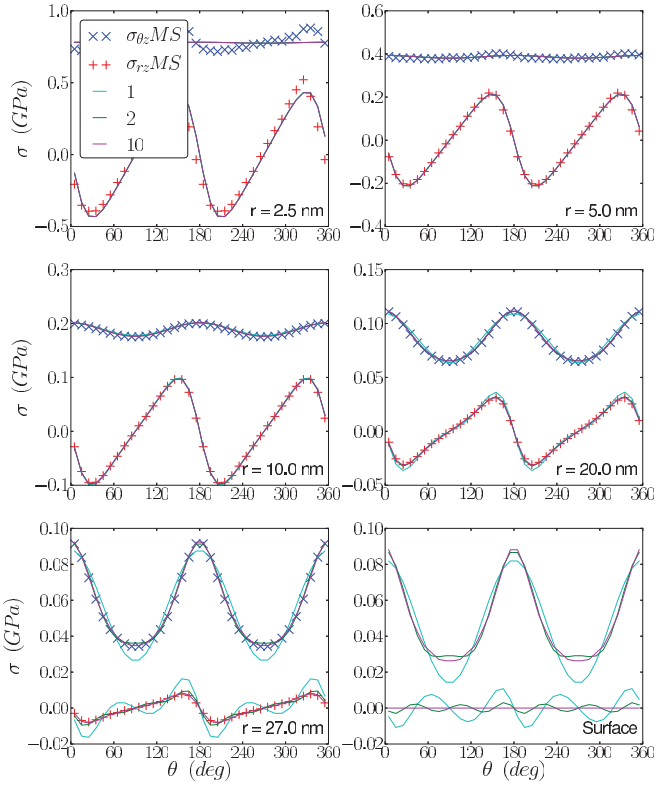

FIG. 7. (Color online) $\sigma_{\theta z}$ ($\times$) and σ_{rz} ($+$) stress components (in GPa) calculated from our atomistic simulation at different r values in the case of an untwisted circular nanowire of radius $R = 30$ nm. These results are compared to the $\sigma^{\infty}_{\theta z} + \sigma^{\text{img}}_{\theta z}$ and $\sigma^{\infty}_{rz} + \sigma^{\text{img}}_{rz}$ terms that are derived from the expression of displacement field $u^{\infty}_z + u^{\text{img}}_z$ written in Eq. (19). Different truncations of the series $N = 1,2,10$ are considered. The $A(n)$ Fourier coefficients are adjusted in order to cancel the traction on the lateral surface.

different radii of the untwisted nanowire. The good agreement between the Fourier analysis based on Eq. (19) and the direct calculation of the stress per atom from our simulations (i.e., from the atomic relaxed positions and the SMA potential) is found as soon as r is greater than 50 Å and for a number of harmonics $n \geqslant 2$ in Eq. (19). For a smaller $r = 25$ Å in Fig. 7, some discrepancy can be noticed due to the dissociation of the dislocation core. On the other hand, at the surface in Fig. 7, an infinite number of harmonics is necessary to reproduce exactly the vanishing traction.

We conclude from the above Fourier analysis that the stress field calculated in our atomistic simulations can be rationalized as a solution of a boundary problem in the framework of the anisotropic elasticity theory. Very interestingly, this numerical method is quite general and can be extended to a more complex/realistic cross section shape. For instance, we have successfully treated the case of the equilibrium hexagonal cross section made of two (100) and four (111) lateral facets that minimizes the surface energy of a [011] fcc nanowire (see Fig. 11 in Appendix A). In this case, a new set of Fourier coefficients $A(n)$ is determined leading to the σ^{img}_{rz} and $\sigma^{\text{img}}_{\theta z}$ fields that render null the traction on the six plans delimiting the lateral surface of the untwisted nanowire. It is worth noting that contrary to the circular cross section where the torsion [u_θ in Eq. (13)] does not affect the traction at the surface, the hexagonal case requires a second Fourier analysis to calculate the $\sigma^{\text{twist}}_{\theta z}$ and $\sigma^{\text{twist}}_{rz}$ fields at the Eshelby angle of twist.

Returning to the case of the circular nanowire, it is tempting to propose an analytical form of the atomistic stress fields found in Fig. 7. From Eqs. (2) and (12), let us first rewrite the stress field due to the dislocation in the following compact form:

$$\begin{aligned} \sigma^{\infty}_{rz} &= \frac{\kappa}{r} f(\theta), \\ \sigma^{\infty}_{\theta z} &= \frac{\kappa}{r}, \end{aligned} \tag{20}$$

where $\kappa = b\sqrt{C_{44}C_{55}}/2\pi$ and $f(\theta) = c_{45}(\theta)/c_{44}(\theta)$ with $c_{45}(\theta)$ and $c_{44}(\theta)$ defined in Eq. (2). Considering both the surface condition of Eq. (15) and the equilibrium condition of Eq. (6), a straightforward approximation of the image field is

$$\begin{aligned} \sigma^{\text{img}}_{rz} &\cong -\frac{\kappa r}{R^2} f(\theta) = -\frac{\kappa r}{R^2} \frac{c_{45}(\theta)}{c_{44}(\theta)}, \\ \sigma^{\text{img}}_{\theta z} &\cong -2 \int \sigma^{\text{img}}_{rz} d\theta = -\frac{\kappa r}{R^2} \ln[c_{44}(\theta)/C_0], \end{aligned} \tag{21}$$

where C_0 is to be determined as a combination of the elastic constants C_{44} and C_{55}. In Fig. 8, with $C_0 = C_{55}/2$, we show that the expressions of $\sigma^{\infty}_{rz} + \sigma^{\text{img}}_{rz}$ and $\sigma^{\infty}_{\theta z} + \sigma^{\text{img}}_{\theta z}$ given by Eqs. (20) and (21) capture very well both the r and the θ

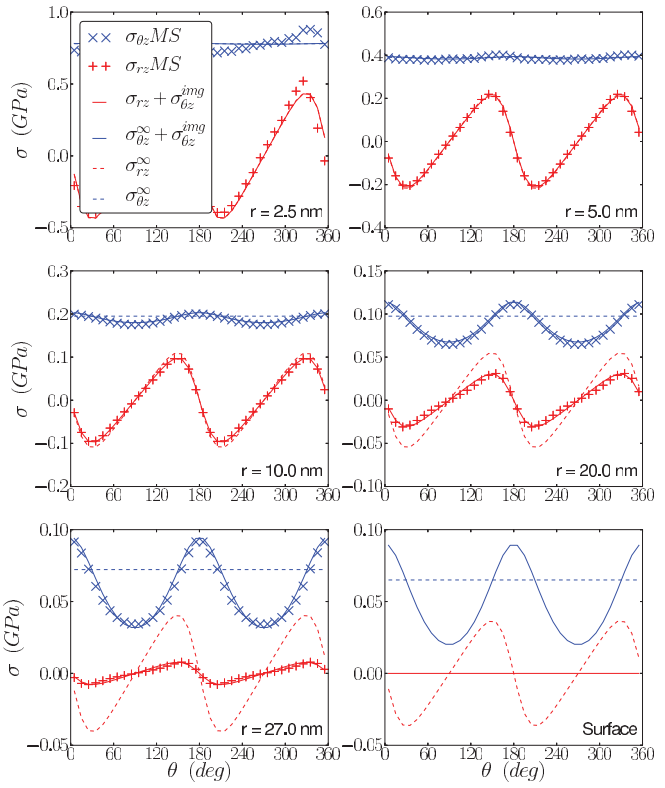

FIG. 8. (Color online) $\sigma_{\theta z}$ ($\times$) and σ_{rz} ($+$) stress components (in GPa) calculated from our atomistic simulation at different r values in the case of an untwisted circular nanowire of radius $R = 30$ nm. These results already shown in Fig. 7 are compared to the expressions of $\sigma^{\infty}_{\theta z} + \sigma^{\text{img}}_{\theta z}$ and $\sigma^{\infty}_{rz} + \sigma^{\text{img}}_{rz}$ (solid lines) proposed in Eqs. (20) and (21). The dotted lines are obtained without the image field by plotting only $\sigma^{\infty}_{\theta z}$ and σ^{∞}_{rz} from Eq. (20).

dependence of the stress fields measured in the atomistic simulations. Furthermore, by considering various nanowires with radius R ranging from 6 to 30 nm, we also verified that the $1/R^2$ law in Eq. (21) is well obeyed. Finally, one may wish to improve the approximation made in Eq. (21). This is possible by considering again a series of additional terms in the image fields whose role is to fulfill the compatibility condition of Eq. (17).

The last question we wish to elucidate in this section is the interpretation of the displacement fields u_z shown in Fig. 6 in the case of the free (twisted) [011] circular nanowire containing the screw dislocation. Indeed, if the image stress field is now well understood from both the Fourier analysis and from our analytical derivation, one may wonder if the solution envisaged in Eq. (19) is also consistent with the displacements found in our atomistic simulations. To verify this latter point, we replot in Figs. 9(a) and 9(b), the two displacement fields denoted $u_z^{\infty} + u_z^{\text{img}} - u_z^{\infty,i}$ and u_z^{twist} [already shown respectively in Figs. 6(b) and 6(c)] that constitute the complete solution of the free nanowire [in Fig. 6(d)]. By using the same set of Fourier coefficients established previously in the stress field study, one also obtains a good modeling of the displacement field in Fig. 9(a) using Eq. (19). Besides in Fig. 9(b), one can notice that the classical warping function of Eq. (13) expected from the torsion of a pure orthotropic bar also agrees well with our atomistic observation. To summarize, we confirm in this section that the displacement field u_z in a free nanowire containing the screw dislocation can be seen as

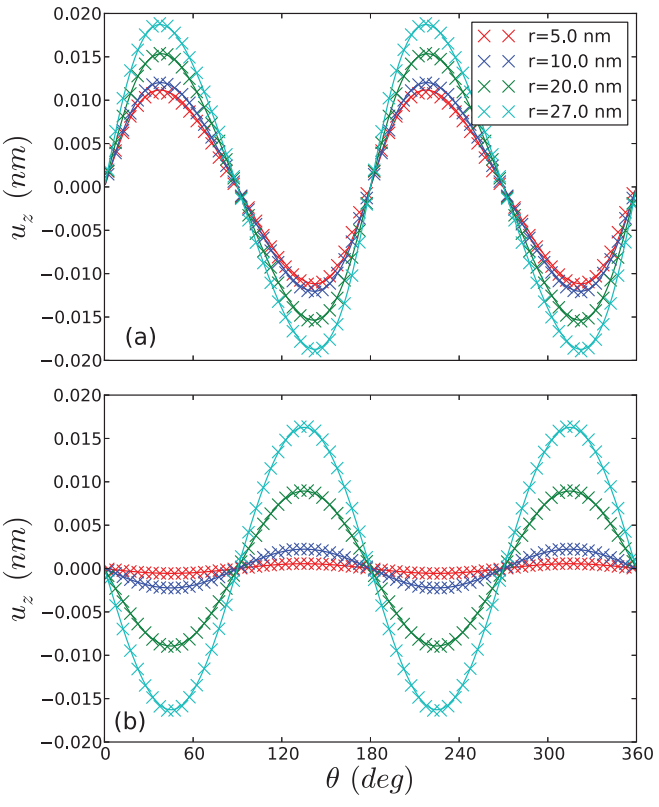

FIG. 9. (Color online) Angular and radius dependence of the displacement field u_z reproduced from Figs. 5(b) and 5(c) (with $\times$ symbols) and compared to (a) $u_z^{\infty} + u_z^{\text{img}}$ in Eq. (19) and (b) u_z^{twist} in Eq. (13) using solid lines.

the superposition of three fields: $u^{\text{tot}} = u_z^{\infty} + u_z^{\text{twist}} + u_z^{\text{img}}$, the latter image field being described by Eq. (19).

Finally, to give a simple representation of the image field u_z^{img} modeled by the series in Eq. (19), it is worth mentioning that u_z^{img} is very close to its first dominant term [i.e., $u_z^{\text{img}} \cong A(1) r_e^2 \sin 2\theta_e = A(1) r^2 \sin 2\theta = 2A(1)xy$] and therefore resembles to another warping function similar to u_z^{twist}. Using energetic arguments, this additional u_z^{img} term can be simply justified. For the sake of clarity, this derivation is given in Appendix B where we also conclude that the energetic contribution of the image field remains small. We will show, however, in the next section that its influence on the x-ray diffraction spectra is significant and cannot be neglected in such experiments.

C. X-ray diffractograms

In his original paper of 1952,[1] Eshelby already considered x-ray diffraction experiments to establish the presence or absence of a dislocation in a whisker. At that time, only the diffraction pattern caused by the isotropic displacement $u_z^{\infty,i} = b\theta/2\pi$ was known from Wilson calculations.[29,30] Nowadays, it becomes possible to perform coherent x-ray diffraction on a single nanowire[6,7] and from the atomistic simulations to get a lot of information on the predicted diffractogram.[15] The aim of this section is to investigate the effect on the 044 reflection of each contribution (i.e., anisotropy, dislocation core, surface effects, image effects, twist) to the total u_z field caused by an axial screw dislocation in a [011] circular copper nanowire. This particular reflection was chosen because it is highly sensitive to the u_z component of the displacement field and only to that component (z is along the [011] direction). It can be measured in relatively standard conditions. The same 044 reflection is examined in Appendix A in the case of a Cu nanowire having the equilibrium hexagonal cross section.

In Fig. 10(b), we plot the 044 reflection of the x-ray scattered intensity $I(\mathbf{q})$ obtained by Wilson for a screw dislocation in an isotropic cylinder of radius R.[29] $I(\mathbf{q})$ is described in the kinematic approximation from the calculation of the amplitude $\mathcal{A}(\mathbf{q}) \propto \sum_{\text{atom j}} \exp i\mathbf{q} \cdot \mathbf{r}_j$ where $\mathbf{q}$ is the scattering vector and $I(\mathbf{q}) = |\mathcal{A}(\mathbf{q})|^2$. According to Wilson (Ref. 30), for 0-mm reflection with m even, $\mathcal{A}(q)$ takes the form,

$$\mathcal{A}(q) \propto \frac{-2}{\eta} J_{m-1}(\eta) + \frac{2m}{\eta^2}\left(1 - J_0(\eta) - 2\sum_{g=1}^{\frac{m}{2}-1} J_{m-2g}(\eta)\right), \tag{22}$$

where $q = |\mathbf{q}|$, $\eta = qR$ and $J's$ are Bessel functions of the first kind. This solution formulated in Eq. (22) serves as a valuable reference since we can numerically verify that the same $I(\mathbf{q})$ diffractogram is obtained in our simulation box from a circular untwisted cylinder where Cu atoms are displaced according to $u_z^{\infty,i}$ [Fig. 10(b)]. This classical isotropic result is, however, nontrivial and should be compared to the well-known Airy pattern plotted in Fig. 10(a) from a perfect circular nanowire with $u_z = 0$ or equivalently from the 000 reflection [$m = 0$ in Eq. (22)]. Indeed, starting from the Airy pattern in Fig. 10(a) made of concentric rings around a central spot, two important

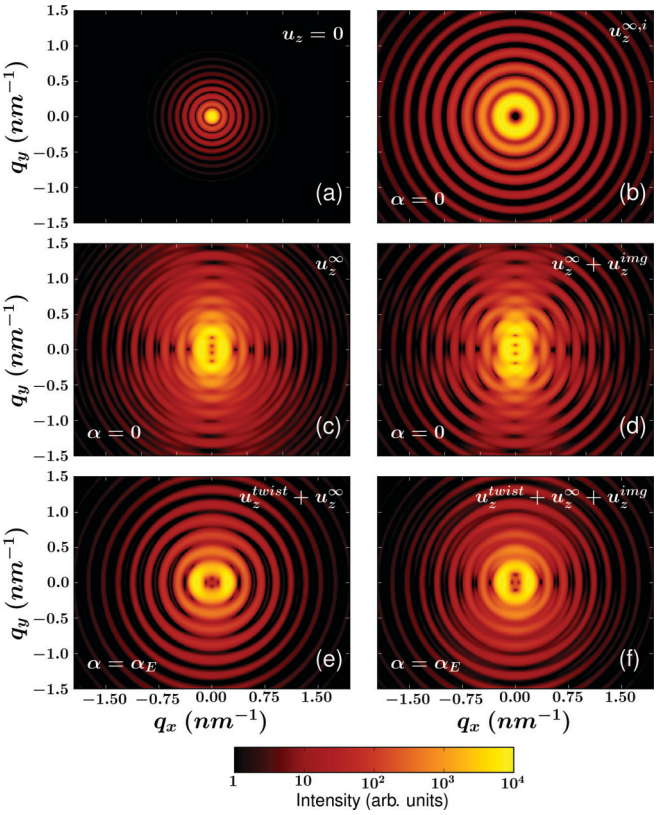

FIG. 10. (Color online) (q_x, q_y) reciprocal space map around the 044 reflection in the case of a circular nanowire of radius $R = 30$ nm with q_x and q_y being the components of the scattering vector $\mathbf{q}$ along $[100]^*$ and $[01\bar{1}]^*$, respectively: (a) $u_z = 0$, Airy pattern; (b) $u_z = u_z^{\infty,i}$, isotropic Wilson solution; (c) $u_z = u_z^{\infty}$, untwisted and no image field; (d) $u_z = u_z^{\infty} + u_z^{\text{img}}$, effect of the image field; (e) $u_z = u_z^{\infty} + u_z^{\text{twist}}$, twisted and no image field; (f) $u_z = u_z^{\infty} + u_z^{\text{twist}} + u_z^{\text{img}}$, total displacement field including the image field.

modifications are observed in the presence of the dislocation at the 044 reflection. First, destructive interference occurs for $q = 0$ in Fig. 10(b) and secondly the additional $1 - J_0(\eta)$ term that appears in Eq. (22) for $m \neq 0$, leads to an apparent doubling of the spacing between rings.

The diffraction pattern is even more complex in Fig. 10(c) when the 044 reflection arises from the anisotropic displacement field $u_z^{\infty} = b\theta_e/2\pi$. Anisotropy strongly changes the reciprocal space map [Fig. 10(c)] when compared to the isotropic one. The central intense spot becomes oval, contains now four distinct aligned extinction points and is surrounded by a sophisticated assembly of portions of rings preserving the symmetry two of the [011] nanowire. Interestingly, we can also affirm that the dissociation of the perfect screw dislocation into two partials has no effect on the 044 reflection since by subtracting in our atomistic simulations the image field u_z^{img} elucidated in Sec. III B from Eq. (19), one gets the same diffractogram shown in Fig. 10(c) of a perfect dislocation. On the other hand, if one keeps u_z^{img} in the calculation of $I(\mathbf{q})$, Fig. 10(d) shows noticeable differences due to the surface image field.

Furthermore, by adding in the system the torsion field u_z^{twist} [in Eq. (13)] that produces the Eshelby twist (for $\alpha = \alpha_E$), most of the previous details ascribed to the anisotropy are attenuated by the torsion. This is related to the fact that in a large part of the diffracting volume (for $200 < r < 300$ Å) the absolute displacement field with torsion tends to the isotropic one as seen in Fig. 6(d). With torsion but by removing the image field in Fig. 10(e), the 044 reflection is closer to the Wilson isotropic case found in Fig. 10(b) with some differences that mainly concern the shape of the central spot. The last Fig. 10(f) closes this section since it gives the importance of the image field u_z^{img} resolved in the present work on the 044 reflection. In comparison to Fig. 10(e), clear signatures of the image field are visible in Fig. 10(f). In particular, the apparent rotation of the central spot and the presence of diffuse arcs of circles should be seen experimentally. However, depending on the experimental conditions, Cu nanowires might already present facets forming an equilibrium hexagonal cross section. This more realistic situation depicted in Appendix A shows similar properties of the 044 reflection even though the 000 reflection is already more complicated. In short, the torsion tends to counterbalance the anisotropy effect and gives an x-ray pattern similar to the isotropic case while the image field should be evidenced from its influence on the shape of the central spot and on the splitting of the truncation rods.

Among the six calculated diffraction patterns shown in Fig. 10, two might be obtained experimentally [i.e., Figs. 10(a) and 10(f)] if the necessary conditions of high resolution and intensity are fulfilled. The pixel size of Figs. 10 and 12 correspond to a reciprocal space resolution of 7.5 10^{-4} Å^{-1}. This resolution can be achieved, for example, at a standard energy of 12 keV with an x-ray camera having a pixel size of 100 microns at a distance of approximately 0.8 m from the sample. These characteristics, or similar characteristics can be obtained at many synchrotron facilities. For example, the resolution reported by Vaxelaire *et al.* (Ref. 31) at an energy very close to 12 keV and Jacques *et al.* (Ref. 8) at a lower energy are, respectively, 1.1 10^{-4} Å^{-1} and 1.5 10^{-4} Å^{-1} (i.e., 7 and 5 times better). The diffracted intensity of a nanowire increases with its diameter and the atomic number of its elements. Experiments have been already reported on a nanowire made of Si (lighter than Cu) with a radius close to the one considered in Fig. 10.[32] In conclusion, considering both intensity and resolution, the diffracted patterns of Figs. 10(a) and 10(f) should be accessible experimentally. This is also true for the two diffracted patterns of Figs. 12(a) and 12(f) in Appendix A.

IV. CONCLUSION

By performing intensive atomistic simulations with a tight-binding potential we have studied the u_z displacement field and the resulting σ_{rz} and $\sigma_{\theta z}$ stress components induced by a metastable axial screw dislocation lying along a [011] copper nanowire with a circular cross section. All the parameters participating in this so-called boundary problem are examined: the elastic anisotropy due to the twofold [011] nanowire orientation, the dislocation core dissociation, the Eshelby twist that stabilizes the dislocation, the surface stress, and the influence of the cross-section shape. Our findings in the present work are the following:

(i) The generalized Young-Laplace GYL equations [in Eq. (4)] that give the relation between surface stress and bulk

stress near the surface are verified in our simulations. Only the third GYL equation involves σ_{rz} but it is shown that the influence of the surface stress on this latter component can be neglected for R ranging from 6 to 30 nm.

(ii) As a consequence, the image displacement field found in our simulations can be analyzed by imposing the classical free traction conditions on the lateral surface. The boundary problem is then resolved numerically from a Fourier series analysis giving both the displacement and stress fields in very good agreement with our atomistic calculations. This method is extended with success to the equilibrium hexagonal cross section. The only discrepancy is found near the core of the dislocation where as expected, the u_z expression chosen in the present analysis is too simple to reproduce the dissociation. In the case of the circular cross section, the Fourier analysis is completed by proposing an approximate analytical solution of the image stress field in Eq. (21). Finally, we show using energetic arguments that the gain in energy due to the image displacement field is mostly contained in the first term of the Fourier series (i.e., the $r^2 \sin 2\theta$ term) and is independent of the torsion.

(iii) In the last part of this work, we wonder if the image displacement field could be seen experimentally from x-ray diffraction experiments. A detailed examination of the reciprocal space map around the 044 reflection points out clear signatures of the image field for both the circular and the hexagonal cross sections.

Thus, the present work should help analyzing future x-ray experiments. Furthermore, it provides a useful theoretical framework to investigate other issues of the Eshelby twist like, for instance, the question of the stability of the screw dislocation in a nanowire.

ACKNOWLEDGMENTS

This research was supported by the ANR under Grant No. ANR-11-BS10-01401 MECANIX.

APPENDIX A: EQUILIBRIUM HEXAGONAL CROSS SECTION

For the sake of clarity, we report separately in this appendix the Fourier analysis of the stress components $\sigma_{\theta z}$ and σ_{rz} caused by a screw dislocation in an untwisted nanowire having an equilibrium hexagonal cross section made of {100} and {111} facets that minimize the surface energy of the nanowire (see the inset of Fig. 11). The area of the cross section is maintained equal to the one of the circular nanowire of radius $R = 30$ nm. Let us recall that as soon as the cross section is not circular, the stress field due to the torsion also leads to nonvanishing $\sigma_{\theta z}^{\text{twist}}$ and $\sigma_{rz}^{\text{twist}}$ stress components presenting harmonics. Thus, to treat the complete case of a twisted nanowire with dislocation, a second Fourier analysis is performed (in addition to the one shown in Fig. 11) to get the amplitudes of the harmonics due to the torsion of a hexagonal nanowire free of dislocation. The addition of the two series gives the full stress field due to both the dislocation and the torsion. As a consequence in Fig. 12, we keep the notation u_z^{img} for defining the displacement image field in the

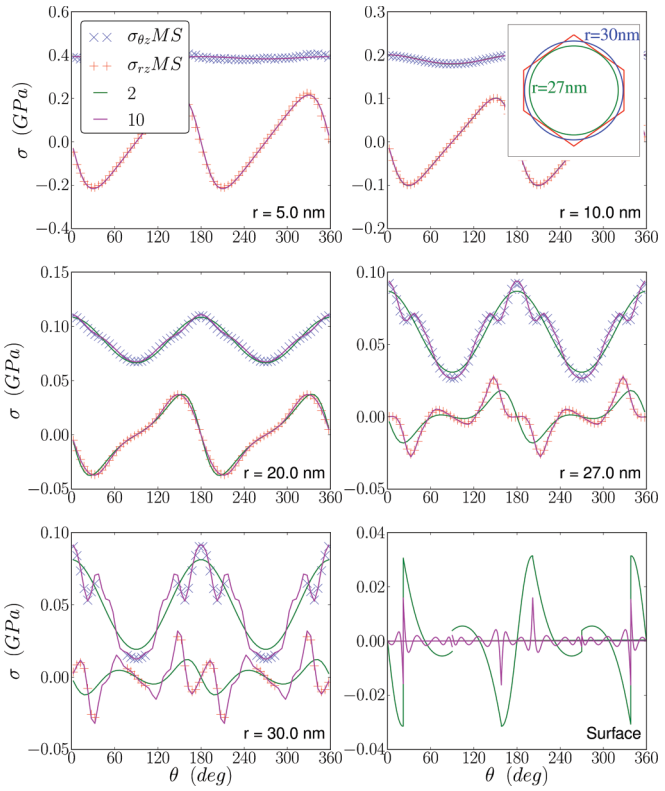

FIG. 11. (Color online) $\sigma_{\theta z}$ (×) and σ_{rz} (+) stress components (in GPa) calculated from our atomistic simulation at different r values in the case of an untwisted hexagonal nanowire. These results are compared to the $\sigma_{\theta z}^{\infty} + \sigma_{\theta z}^{\text{img}}$ and $\sigma_{rz}^{\infty} + \sigma_{rz}^{\text{img}}$ terms that are derived from the expression of the displacement field $u_z^{\infty} + u_z^{\text{img}}$ written in Eq. (19). Two truncations of the series $N = 2,10$ are shown. The $A(n)$ Fourier coefficients are adjusted in order to cancel the traction on the lateral {100} and {111} facets. The stress singularities related to the surface edges are visible.

untwisted case, but u_z^{twist} is now different from Eq. (13) and is a new warp associated with the twist of the hexagonal cylinder. Again clear signatures of the image field u_z^{img} are observed in Fig. 12 where various reciprocal space maps around the 044 reflection are calculated for different displacement fields in the hexagonal nanowire.

APPENDIX B: ENERGY GAIN DUE TO THE IMAGE FIELD

To interpret from energetic arguments the image field u_z^{img} found in this work, we retain its first-order term $u_z^{\text{img}} \cong 2A(1)xy$ in Eq. (19). Let us then write the displacement field in Cartesian coordinates:

$$\begin{aligned} u_x &= -\alpha yz, \\ u_y &= \alpha xz, \\ u_z &= u_z^{\infty} + u_z^{\text{img}} + u_z^{\text{twist}} \\ &\cong u_z^{\infty} + A_1 xy - \alpha \frac{C_{\ominus}}{C_{\oplus}} xy, \end{aligned} \tag{B1}$$

where α is the twist and $A_1 = 2A(1)$ the amplitude of the image field to be determined, $C_{\oplus} = (C_{44} + C_{55})/2$ and

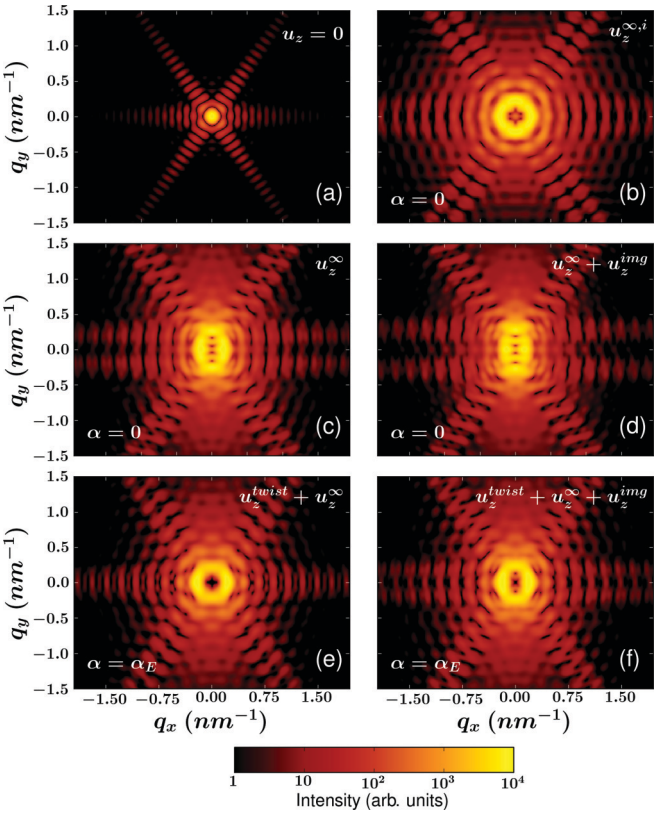

FIG. 12. (Color online) (q_x, q_y) reciprocal space map around the 044 reflection in the case of a hexagonal nanowire of radius $R = 30$ nm with q_x and q_y being the components of the scattering vector $\mathbf{q}$ along $[100]^*$ and $[01\bar{1}]^*$, respectively: (a) $u_z = 0$; (b) $u_z = u_z^{\infty,i}$, isotropic solution; (c) $u_z = u_z^{\infty}$, untwisted and no image field; (d) $u_z = u_z^{\infty} + u_z^{\text{img}}$, effect of the image field; (e) $u_z = u_z^{\infty} + u_z^{\text{twist}}$, twisted and no image field; (f) $u_z = u_z^{\infty} + u_z^{\text{twist}} + u_z^{\text{img}}$, total displacement field including the image field.

$C_{\ominus} = (C_{44} - C_{55})/2$. The part of the elastic energy per unit length U^* that depends on the strain components $\epsilon_{zx} = \frac{1}{2}(\frac{\partial u_z}{\partial x} + \frac{\partial u_x}{\partial z})$ and $\epsilon_{zy} = \frac{1}{2}(\frac{\partial u_z}{\partial y} + \frac{\partial u_y}{\partial z})$ estimated from Eq. (B1) can then be expressed as

$$\begin{aligned} U^*(A_1,\alpha) &= \iint 2\left(C_{44}\epsilon_{zy}^2 + C_{55}\epsilon_{zx}^2\right)dxdy \\ &= \iint \frac{C_{44}x^2}{2}\left(\frac{\kappa}{C_{44}x^2 + C_{55}y^2} + A_1 + \alpha\frac{C_{55}}{C_{\oplus}}\right)^2 dxdy \\ &\quad + \iint \frac{C_{55}y^2}{2}\left(\frac{\kappa}{C_{44}x^2 + C_{55}y^2} - A_1 + \alpha\frac{C_{44}}{C_{\oplus}}\right)^2 dxdy \\ &= U^*(0,0) + I_1A_1 + \frac{I_2}{2}A_1^2 + I_3\alpha + \frac{I_4}{2}\alpha^2 + I_5A_1\alpha, \end{aligned} \tag{B2}$$

where the integrals I_n write

$$I_1 = \kappa \iint \frac{C_{44}x^2 - C_{55}y^2}{C_{44}x^2 + C_{55}y^2}dxdy = \kappa\pi R^2\frac{(1-\sqrt{C_{\oslash}})}{(1+\sqrt{C_{\oslash}})},$$

$$I_2 = \iint (C_{44}x^2 + C_{55}y^2)dxdy = \frac{\pi R^4}{2}C_{\oplus},$$

$$I_3 = \kappa\frac{C_{\otimes}}{C_{\oplus}} \iint \frac{x^2+y^2}{C_{44}x^2 + C_{55}y^2}dxdy = \frac{bR^2}{2}\frac{C_{\otimes}}{C_{\oplus}},$$

$$I_4 = \frac{C_{\otimes}}{C_{\oplus}^2}I_2 \quad \text{and} \quad I_5 \propto \iint (x^2 - y^2)dxdy = 0,$$

with $\kappa = b\sqrt{C_{44}C_{55}}/2\pi$, $C_{\otimes} = C_{44}C_{55}$, and $C_{\oslash} = C_{55}/C_{44}$.

Since I_5 is null, we recover that the angle of twist α_E minimizing U^* does not depend on the amplitude of the image field A_1. Moreover from Eq. (B2), we verify that the gain in energy $\Delta U_{\text{torsion}}$ due to the torsion is maximum for

$$\alpha = -\frac{I_3}{I_4} = -\frac{b}{\pi R^2} = \alpha_E, \tag{B3}$$

and does not depend on R:

$$\Delta U_{\text{torsion}} = -\frac{I_3^2}{2I_4} = -\frac{b^2}{4\pi}\frac{C_{\otimes}}{C_{\oplus}}, \tag{B4}$$

a result that is consistent with the isotropic solution where $C_{44} = C_{55}$.[1] On the other hand, if one examines now the energy gain induced by the image field ΔU_{image}, a maximum of gain is reached for

$$A_1 = -\frac{I_1}{I_2} = -\frac{2\kappa}{R^2C_{\oplus}}\frac{(1-\sqrt{C_{\oslash}})}{(1+\sqrt{C_{\oslash}})}, \tag{B5}$$

where $C_{\oslash} = C_{55}/C_{44}$ and corresponds to a reduction of the energy:

$$\Delta U_{\text{image}} = -\frac{I_1^2}{2I_2} = -\frac{b^2}{4\pi}\frac{C_{\otimes}}{C_{\oplus}}\frac{(1-\sqrt{C_{\oslash}})^2}{(1+\sqrt{C_{\oslash}})^2}. \tag{B6}$$

Numerically for $R = 30$ nm, the twist obtained at equilibrium is $-9.0968\ 10^{-6}$ rad/Å in our simulations as mentioned previously and corresponds well to the α_E value $-9.069\ 10^{-6}$ rad/Å in Eq. (B3). For this state of torsion, the energy gain $\Delta U_{\text{torsion}}$ is 0.1345 eV/Å as expected from the theoretical value in Eq. (B4). Notice that according to our simulations the presence (or not) of the dislocation does not affect significantly $\Delta U_{\text{torsion}}$ that is equal to 0.1335 eV/Å without the dislocation. Concerning now the image field, we observe that the amplitude of the displacement field is well described by its first-order term since Eq. (B5) predicts an amplitude $A_1 = 0.172/R^2\text{Å}^{-1}$ while we find $A_1 = 0.19/R^2\text{Å}^{-1}$ from our simulations for R radii ranging from 6 to 30 nm. Finally, the comparison of Eqs. (B4) and (B6) shows that $\Delta U_{\text{torsion}}$ is much larger than ΔU_{image} by a factor close to 14.4 for copper with $\Delta U_{\text{image}} = 0.00942$ eV/Å. This ratio $\Delta U_{\text{torsion}}/\Delta U_{\text{image}} = (1+\sqrt{C_{\oslash}})^2/(1-\sqrt{C_{\oslash}})^2$ decreases slowly when $C_{\oslash} = C_{55}/C_{44}$ increases.

[1] J. D. Eshelby, J. Appl. Phys. **24**, 176 (1952).
[2] J. D. Eshelby, Philos. Mag. **3**, 440 (1958).
[3] J. D. Eshelby, in *Dislocations in Solids*, edited by F. R. N. Nabarro (North-Holland, Amsterdam, 1979), Vol. 1, pp. 167–221.
[4] J. Hirth and J. Lothe, *Theory of Dislocations*, 2nd ed. (John Wileys and Sons, New York, 1982).
[5] M. J. Bierman, Y. K. A. Lau, A. V. Kvit, A. L. Schmitt, and S. Jin, Science **320**, 1060 (2008).

[6]A. Diaz, C. Mocuta, J. Stangl, B. Mandl, C. David, J. Vila-Comamala, V. Chamard, T. H. Metzger, and G. Bauer, Phys. Rev. B **79**, 125324 (2009).
[7]E. Fohtung, J. W. Kim, K. T. Chan, R. Harder, E. E. Fullerton, and O. G. Shpyrko, Appl. Phys. Lett. **101**, 033107 (2012).
[8]V. L. R. Jacques, D. Carbone, R. Ghisleni, and L. Thilly, Phys. Rev. Lett. **111**, 065503 (2013).
[9]G. Richter, K. Hillerich, D. S. Gianola, R. Monig, O. Kraft, and C. A. Volkert, Nano Lett. **9**, 3048 (2009).
[10]C. R. Weinberger and W. Cai, Nano Lett. **10**, 139 (2010).
[11]T. Rasmussen, K. W. Jacobsen, T. Leffers, and O. B. Pedersen, Phys. Rev. B **56**, 2977 (1997).
[12]V. Rosato, M. Guillopé, and B. Legrand, Philos. Mag. A **59**, 321 (1989).
[13]F. Ducastelle, J. Phys. (Paris) **31**, 1055 (1970).
[14]J. Creuze, F. Berthier, R. Tétot, and B. Legrand, Phys. Rev. B **62**, 2813 (2000).
[15]J.-M. Roussel, S. Labat, and O. Thomas, Phys. Rev. B **79**, 014111 (2009).
[16]L. Proville and S. Patinet, Phys. Rev. B **82**, 054115 (2010).
[17]Y. Mishin, M. J. Mehl, D. A. Papaconstantopoulos, A. F. Voter, and J. D. Kress, Phys. Rev. B **63**, 224106 (2001).
[18]M. Chassagne, M. Legros, and D. Rodney, Acta Mater. **59**, 1456 (2011).
[19]W. Cai, W. Fong, E. Eisen, and C. R. Weinberger, J. Mech. Phys. Solids **56**, 3242 (2008).
[20]J. Wortman and R. Evans, J. Appl. Phys. **36**, 153 (1965).
[21]G. Simmons and H. Wang, *Single Crystal Elastic Constants and Calculated Aggregated Properties* (MIT Press, Cambridge, 1971).
[22]M. H. Sadd, *Elasticity: Theory, Applications and Numerics* (Academic Press, Waltham, 2009).
[23]M. Gurtin and A. Murdoch, Ach. Rat. Mech. Anal. **57**, 291 (1975).
[24]P. Sharma, S. Ganti, and N. Bhate, Appl. Phys. Lett. **82**, 535 (2003).
[25]W. Zhang, T. Wang, and X. Chen, J. Appl. Phys. **103**, 123527 (2008).
[26]T. Chen, M.-S. Chiu, and C.-N. Weng, J. Appl. Phys. **100**, 074308 (2006).
[27]S. Olivier, G. Tréglia, A. Saúl, and F. Willaime, Surface Science **600**, 5131 (2006).
[28]P. Muller and A. Saúl, Surf. Sci. Rep. **54**, 157 (2004).
[29]A. J. C. Wilson, Acta Cryst. **5**, 318 (1952).
[30]A. J. C. Wilson, Nuovo Cimento **1**, 277 (1955).
[31]N. Vaxelaire, H. Proudhon, S. Labat, C. Kirchlechner, J. Keckes, V. Jacques, S. Ravy, S. Forest, and O. Thomas, New J. Phys. **12**, 035018 (2010).
[32]V. Favre-Nicolin, J. Eymery, R. Koester, and P. Gentile, Phys. Rev. B **79**, 195401 (2009).